Did Earth have a late veneer? Determining the behaviors of highly siderophile elements during core formation

Jack Sheehan

1 Introduction

Late accretion—the addition of material following planetary core segregation—plays a crucial role in producing a habitable planet (Morbidelli & Wood, 2015; Siebert & Shahar, 2015). The late veneer is a specific hypothesis of late accretion that suggests ~0.007 Earth masses (M_E) were accreted in the form of chondritic meteorites following the last giant impact and the cessation of core formation (Chou, 1978; Walker, 2009). This hypothesis is invoked to explain the dichotomy between the relatively high observed abundances of highly siderophile elements (HSEs) in the bulk silicate Earth (BSE) and the lower abundances predicted by metal–silicate partitioning experiments and core formation models (Chou, 1978; Kimura et al., 1974). Compared to the predicted abundances, observed BSE HSE abundances are ~5 orders of magnitude too high, and in similar relative proportions to chondrites (Siebert & Shahar, 2015).

The late veneer is necessary to account for this difference if we assume the predicted HSE BSE abundances are correct, and it additionally explains their near-chondritic ratios. However, these predicted abundances are primarily based on partitioning experiments at 1 bar or only moderately high pressures (P) and temperatures (T). A pioneering recent study (Suer et al., 2021) has suggested that one HSE, Pt, may become less siderophile at the higher P–T conditions of Earth's core formation. With data on only one element, it is impossible to make any robust comparisons to the observed chondritic relative abundances of HSEs in the BSE, or to place constraints on the late veneer mass required to explain these abundances. Thus, investigating the remaining HSEs—Au, Ir, Os, Pd, Re, Rh, and Ru—could play a key role in chemically tracing late accretion.

I propose to reassess the mass and nature of Earth's late veneer by studying the metal–silicate partitioning behaviors of four HSEs that are expected to display a similar decrease in siderophility, as determined by trends extrapolated from the moderately high P–T metal–silicate partitioning data in the literature: Au, Ru, Rh, and Re (Brenan et al., 2016). These experiments will be run in the laser-heated diamond anvil cell (LH-DAC) at much higher P–T to better understand the role of core formation conditions in shaping their BSE abundances. To apply these mineral physics experiments to questions of planetary scale, I will input the results into a state-of-the-art core formation model paired with Solar System evolution simulations.

Understanding the final stages of planetary accretion is important to evaluate primitive core and mantle compositions, which will help us better characterize the delivery of volatiles and constrain early planetary habitability (Palme & O'Neill, 2013; Righter & O'Brien, 2011; Rubie et al., 2011). This proposal uses Earth as a case study due to the profusion of geochemical data available in the literature, but our results will apply to late accretion in general and may be utilized to evaluate other planets in further studies.

The proposed experimental and computational work will address two main scientific questions:

1. How do the partition coefficients of HSEs change with P, T, and other variables, and how do HSEs partition between metal and silicate at Earth's core formation conditions?
2. Can core formation alone explain the observed absolute and relative BSE HSE abundances, or is a late veneer and/or other process(es) required? What is the minimum late veneer mass needed to explain these observations?

2 Background

2.1 Planetary Accretion

Building a terrestrial planet involves many sequential growth steps, including the accretion of dust, pebbles, planetesimals, and planetary embryos (Jacobson & Walsh, 2015; Morbidelli et al., 2012). Formation begins in the nebular disk, where dust grains settle at the disk mid-plane before coagulating to form pebbles and boulders. From here, planetesimals on the order of kilometers form, gravitationally triggered by locally high concentrations of solids in the disk (Jacobson & Walsh, 2015). These regions of collapsing particles grow rapidly but form sporadically, each carrying a unique signature of the radial and temporal chemical distributions in the disk (Lichtenberg et al., 2022).

Planetesimals continue to grow through mutual collisions before runaway growth turns the largest planetesimals into planetary embryos through gravitational interactions with the population of smaller planetesimals (Chambers, 2001). These different-sized bodies interact through dynamical friction, which dampens the eccentricities of the largest while exciting the neighboring smallest (Morbidelli et al., 2012). The faster, smaller bodies are now more likely to fragment than merge upon colliding, which furthers the effectiveness of dynamical friction (O'Brien et al., 2006). Runaway growth is eventually slowed because the excited eccentricities cause the remaining smaller planetesimals to scatter, depleting the potential local stock of material to grow each embryo further (Jacobson & Walsh, 2015).

When compared to the terrestrial planets, these protoplanets are too numerous, too small, and too homogeneous; a significant, chaotic giant impact stage is required. This is brought about due to gravity perturbations caused by a combination of the formation of the gas giants, the decrease in dynamical friction, and the loss of the stabilizing nebular gas (Chambers & Cassen, 2002). During this excited stage, most of the embryos and remaining planetesimals are lost from the system, while the rest collide in the inner Solar System to form the terrestrial planets (O'Brien et al., 2006). This final stage accounts for the necessary increase in size and radial mixing of the remaining bodies.

Meanwhile, differentiation—the subdivision of a body into physically and chemically distinct layers—occurs simultaneously with accretion within the embryos and some planetesimals. In fact, many of the physical and chemical mechanisms of core formation depend on the accretion scenarios (Fischer et al., 2017). For example, the physical rate of core–mantle segregation depends on the volume of impact-generated melt (Nakajima et al., 2021) and the process of descent through the solid lower mantle (Deguen et al., 2011). In turn, the chemical signature of core–mantle segregation depends on the physical rate of segregation (Nimmo & Kleine, 2015), in addition to the fraction of the impactor core that equilibrates (Fischer et al., 2017) and the partitioning behaviors of the major, minor, and trace elements (Rubie et al., 2011).

Following the giant impact stage and, therefore, core formation, late accretion is defined as the final remaining impacts of planetesimals (Morbidelli & Wood, 2015). These impacts would necessarily be small enough not to cause large-scale remelting, which would restart core formation. In the case of the Earth, the last giant impact is thought to be the Moon-forming impact (Canup, 2004), which means that any impacts following this constitute late accretion. The mass of late-accreted material is debated, but often considered small relative to the Earth (0.001–0.01 M_E) (Brenan & McDonough, 2009; Marchi et al., 2018; Raymond et al., 2013; Walker, 2009). However, because it comes after the end of the most active period of planetary formation, late accretion is considered to have had a disproportionately large effect on the early Earth's

environment. Better characterizing the mass and composition of late-accreted material is therefore an important part of understanding our planet's history and habitability.

2.2 HSEs and the Late Veneer Hypothesis

During differentiation, denser molten iron from the accreting bodies sinks through the less dense molten silicate to the protoplanet's center to form the core (Deguen et al., 2011). As it sinks, the metal reacts with the silicate, allowing for the partitioning of major, minor, and trace elements between the two phases (Rubie et al., 2003). Partitioning behavior is defined by an element's preference for the metallic versus silicate phases, and is expressed in terms of a partition coefficient (D), calculated as:

$$D_M = \frac{X_M^{\text{met}}}{X_M^{\text{sil}}} \quad (1)$$

where X is the mole fraction of the element of interest, M, in the metal and silicate phases. Au, Ir, Os, Pd, Pt, Re, Rh, and Ru are grouped together because they are all highly siderophile, meaning they strongly prefer the iron-rich metallic phase (Kimura et al., 1974; Ringwood, 1966); their experimentally-derived D values fall between 10^4–10^7 (Day et al., 2016). Due to this strong metallic affinity, the HSEs should be almost entirely stripped from the mantle as the iron sinks and segregates.

These elements should therefore be the most depleted of all elements in the BSE. To quantify this, they are compared to the CI chondrite meteorite class (McDonough & Sun, 1995). This benchmark is set by the refractory lithophile elements, which condense at the higher temperatures of Earth's formation and preferentially partition into the BSE during metal–silicate equilibration (Wood et al., 2019). Consequently, the refractory lithophiles are found in the BSE in the same relative proportions as in CI chondrites. This provides a standard to which we can compare other elements, including the HSEs (Figure 1). As expected, the HSEs are strongly depleted in the BSE compared to the other elements. However, when compared to their abundances predicted from their partition coefficients, the observed BSE HSE abundances are orders of magnitude too high (Chou, 1978; Kimura et al., 1974). Additionally, the large range in the HSE partition coefficients should result in significant variation in their depletions, while in actuality the observed BSE HSEs display broadly chondritic ratios (Figure 1) (Chou, 1978).

This apparent excess of HSEs in the BSE is an enduring problem in the fields of geochemistry and planetary science. To date, the most likely hypothesis is the late accretion of a small amount of chondritic material known as the late veneer (Chou, 1978; Kimura et al., 1974). Its small size and late delivery would prevent it from reaching the metal in the segregated core, trapping all the material—including the HSEs—in the

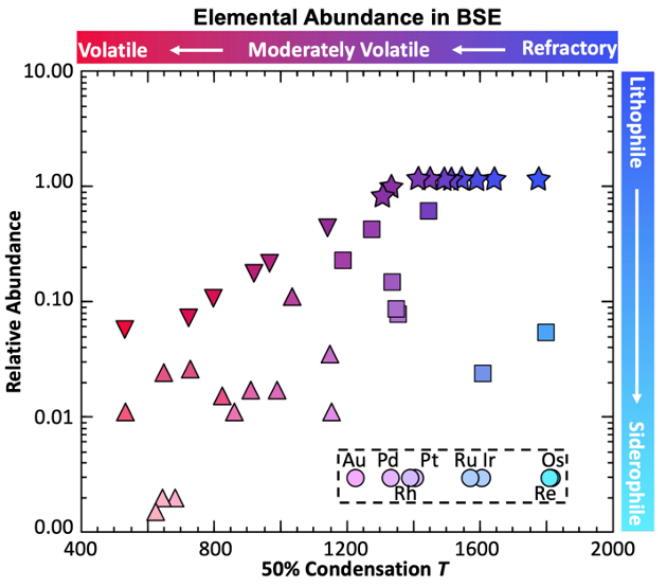

Figure 1. Graph of abundance of elements in the BSE relative to CI Chondrites and normalized to Mg. HSEs are boxed. Modified from Morbidelli & Wood (2015).

mantle. This would explain the excess BSE HSEs by proposing that, despite being mostly stripped from the mantle via metal–silicate partitioning during core formation, they were added later during the late veneer. The late veneer hypothesis also explains the near-chondritic relative ratios of the BSE HSEs. Currently, no core formation conditions have been identified that can reproduce this ratio from metal–silicate equilibration alone (Mann et al., 2012).

Knowing the mantle mass and the proportions of HSEs in various chondrites, a mass balance between the lower predicted BSE HSE contents and the overabundant measured BSE HSE contents can be used to obtain the mass of this late veneer. The modern estimate based on this geochemical approach is ~0.005 M_E (Brenan & McDonough, 2009; Walker, 2009). Further attempts to constrain the late veneer mass using isotopic signatures (e.g., Fischer-Gödde et al., 2020) and dynamical simulations (e.g., Raymond et al., 2013) have yielded similar results, ranging from 0.004 M_E to 0.01 M_E. An area of debate, however, is the size and number of the impactors delivering this late veneer mass. Bottke et al. (2010) proposed accretion of a few large, differentiated (~2,000 km diameter) impactors, while Schlichting et al. (2012) proposed an opposite model of many small (~10 m diameter) impactors. This vast difference in size would have implications for the efficiency of impactor mixing and for the relative late veneer requirements between the terrestrial planets (Brasser et al., 2016; Kendall & Melosh, 2016). Better constraining the mass and nature of the late veneer on Earth could play an important role in furthering our understanding of late accretion throughout the inner Solar System. Because the HSEs serve as chemical tracers of core formation, more accurately defining the late veneer requires more accurately defining the HSE partition coefficients.

2.3 HSE Metal–Silicate Partitioning in the Literature

Many prior studies have postulated that core formation began in planetesimals and continued through the giant impact stage, spanning a wide *P–T* range and reaching a maximum of ~3,000–4,000 K and ~60–100 GPa in the Earth (Fischer et al., 2015; Siebert et al., 2011; Wade & Wood, 2005). At 1 bar and moderate *T*, the HSEs are well studied (for reviews, see Ertel et al., 2008; Walter et al., 2000); it is their behaviors at these conditions that originally led to their "highly siderophile" classification. However, these results require large extrapolations in *P* and *T* to apply to Earth's core formation, introducing significant uncertainties to the predicted partition coefficients.

Over the past two decades, piston–cylinder and multianvil press studies have investigated HSE metal–silicate partitioning up to 23 GPa and ~2800 K (e.g., Bennett, 2013; Bennett et al., 2014; Brenan & McDonough, 2009; Cottrell & Walker, 2006; Danielson et al., 2005; Mann et al., 2012). Important advances in our understanding of HSE partitioning have come from these moderate *P–T* experiments. Most notably, all the HSEs appear to show a strong decrease in siderophility with increasing *T* (Brenan et al., 2016), as is true for most moderately siderophile elements (Fischer et al., 2015). To display these trends, I have fit a representative sample of the HSE metal–silicate partitioning experiments collected from the literature in Figure 2 (see Section 3.3 for methods of fitting).

Attributing a decrease in *D* values to an increase in *P* is more contentious, with different studies offering differing conclusions. Mann et al. (2012) found a relatively strong dependence on *P* (although still weaker than that of *T)* below 6 GPa for Ir, Rh, and Ru, a weaker dependence for Pd and Re, and none for Pt. For Au, Danielson et al. (2005) found a decrease in *D* above 21 GPa. For the majority of studies, however, data across the range of pressures investigated can be reproduced without considering a pressure effect (Brenan et al., 2016). Identifying a potential

influence of P on D is difficult for a variety of reasons. Much of the potential experimental pressure range has not been investigated, which may mask the importance of P at higher values. (Siebert & Shahar, 2015). Additionally, most of the highest P data all come from one study, Mann et al. (2012), making it impossible to independently validate the partitioning behaviors. It is also very difficult to separate P and T within an individual experiment, because the melting curve increases with P. When combined with vastly different oxygen fugacity (fO_2) conditions, changes in silicate melt structures, the intermittent inclusion of sulfur, and the effects of light elements (each of which is discussed further in Section 3.3), this makes comparisons across different P–T values very difficult.

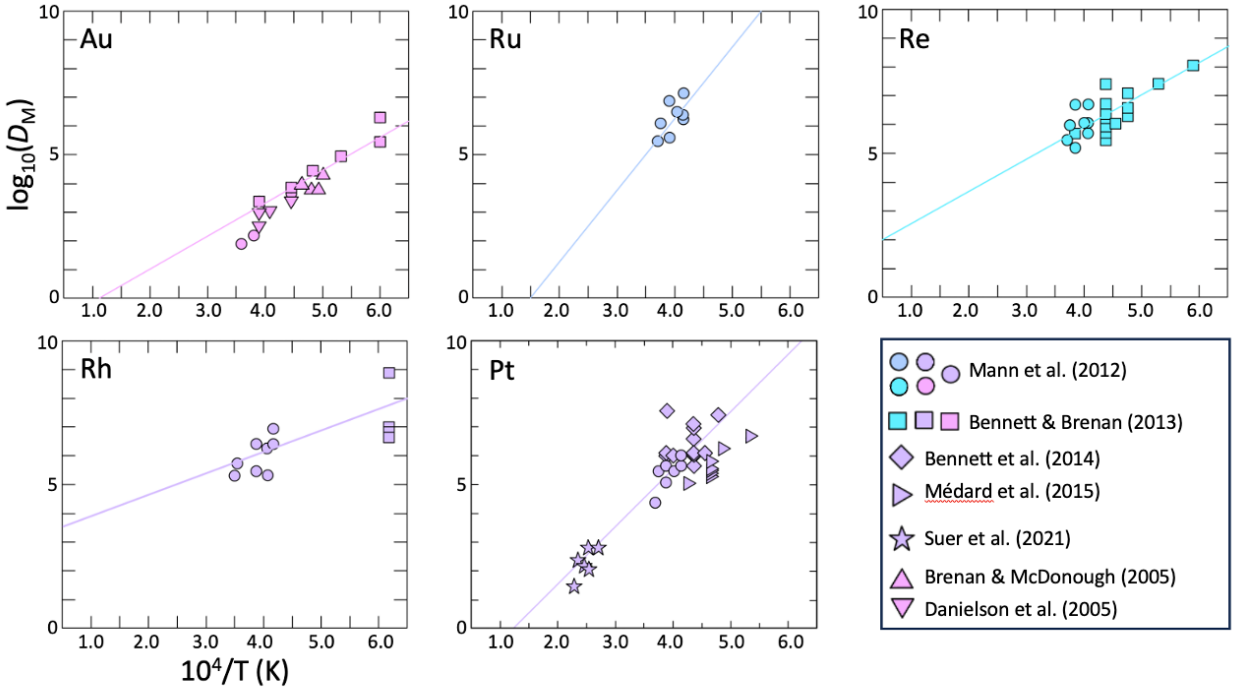

Figure 2. Metal–silicate partition coefficients for the selected HSEs and Pt as a function of inverse temperature. The solid lines are isobaric fits defined for IW–2. Colors correspond to Figure 1. Au) Bennett & Brenan (2013), Brennan & McDonough (2005), Danielson et al. (2005), Mann et al. (2012); Ru) Mann et al. (2012); Re) Bennett & Brenan (2013), Mann et al. (2012); Rh) Ertel et al. (1999), Mann et al. (2012); Pt) Bennett et al. (2014), Mann et al. (2012), Médard et al. (2015), Suer et al. (2021).

The extreme siderophility of the HSEs, combined with issues typical for these types of experiments, has prevented these experimental P–T ranges from being easily replicated or extended. Besides the mechanical limitations of the experimental setups that govern the maximum achievable P and T, the other most common issue cited in HSE metal–silicate partitioning experiments is the formation of metallic inclusions in the silicate. The origins of these features and therefore the proper procedures for analyzing them have long been debated (e.g., Brenan et al., 2016; Cottrell & Walker, 2006; Ertel et al., 2008). Treating these "nuggets" as particles that were present during the experiment versus that only exsolved from the silicate melt upon quench has huge implications for the magnitude of the inferred HSE partition coefficients, because siderophile elements (including the HSEs) are much less abundant in the silicate than in

these nuggets embedded in it. Additionally, a common method of nugget suppression is utilizing relatively high fO_2 compared to conditions relevant to core formation, which limits the extent of fO_2 conditions investigated as a factor affecting HSE partitioning.

To further characterize core formation requires precise understanding of HSE partitioning behaviors across a wide range of conditions, as exemplified in Figure 2. Better defining the regression coefficients that describe their partitioning behaviors requires experimental and analytical advances to investigate the full range of P–T–X–fO_2 space and isolate each parameter's effect on partitioning. Advances in the LH-DAC (Anzellini & Boccato, 2020) and breakthroughs in applying analytical techniques to recovered samples (Fischer et al., 2020; Siebert et al., 2012) have dramatically expanded the P–T range accessible experimentally, eliminating the need for large extrapolations to core formation conditions and providing new results to compare to the lower P–T trends discussed above. Suer et al. (2021) investigated Pt partitioning up to 111 GPa and 4300 K in the LH-DAC, determining that D_{Pt} decreases by a further three orders of magnitude with the high T in this study compared to previous experimental trends at lower T (Figure 2). There is also a growing consensus that the "nanonuggets" found in the silicate melts of LH-DAC experiments exsolve upon quench and should therefore be included in the analysis of the silicate, at least when they are small (e.g., Fischer et al., 2015, 2020; Médard et al., 2015; Suer et al., 2021). Providing similar experimental constraints on the remaining HSEs and further studying the nanonuggets that form in these experiments will result in a vastly improved understanding of their partitioning behaviors at high P–T and consequently more robust evaluations of different core formation and late accretion scenarios.

3 Methodology

3.1 LH-DAC Metal–Silicate Partitioning Experiments

My proposed experiments will take advantage of recent advances in lasers and optics, particularly fortemperature measurement and mapping in the LH-DAC (Anzellini & Boccato, 2020; Bouhifd & Jephcoat, 2011; Campbell, 2008), as well as recent developments in the spatial and analytical resolution of post-run chemical analysis techniques (Fischer et al., 2020; Siebert et al., 2012). I intend to perform at least 20 successful experiments whose chemical compositions can be adequately measured. Even with technological advances, based on previous LH-DAC partitioning studies (e.g., Fischer et al., 2020) I anticipate this will likely involve having to run approximately 40 experiments in total. By utilizing the laser-heating system in the Fischer Lab at Harvard instead of a synchrotron-based system, I can perform as many experiments as necessary, which will greatly benefit a study like this that requires meticulous precision and has a lower inherent success rate for each experiment.

LH-DAC experiments create these P–T conditions by compressing a sample between two diamond anvils. These pressurized samples are then heated from both sides by laser irradiation, which passes through the transparent diamonds and melts a portion of the sample. In the Fischer Lab, two 50 W Yb-doped infrared lasers with 1064 nm wavelength will be used to create a large (~20 μm) spot size, which helps to reduce lateral temperature gradients. Laser power on the two sides of the sample will be adjusted independently to minimize axial temperature gradients. Currently we measure temperature using a spectroradiometric system to record the spectral radiance and wavelength over a desired range. Using the Wien approximation of the Planck law, we fit the thermal radiation spectrum linearly, deriving temperature and emissivity measurements at every time of recording. However, this method only records the temperature at the center of

the laser-heated spot. To quantify any lateral temperature gradients, I will utilize an eight-color temperature measurement system that we are currently building in the Fischer Lab. This system will capture images of the thermal emission from the sample at 400, 460, 532, 600, 700, 770, 850, and 950 nm simultaneously. These eight images will be spatially correlated, and at each pixel, we will fit the eight measurements to the Planck function using the Wien and graybody approximations, allowing for temperature and emissivity mapping across the entire laser-heated spot. This will provide unprecedented analysis of lateral temperature gradients and therefore more accurate temperature determination at the metal–silicate interface where partitioning is occurring, which may differ from the temperature typically measured in the center of the laser-heated spot (Campbell, 2008; Fischer & Campbell, 2010). Temperature uncertainties will be calculated based on an estimated analytical uncertainty, the difference in temperature on the two sides, and a correction for axial temperature gradients as in (Campbell et al., 2007).

Compared to four-color systems such as Campbell (2008), our system will have significantly higher throughput and dynamic range, with measurements at more wavelengths spanning a wider wavelength range. These improvements will allow us to measure a wider range of temperatures, with lower uncertainties, and will reduce the chances of an experiment failing due to inadequate temperature measurements. They will also allow us to measure the temperature distribution more rapidly, which is important due to the large inherent temperature fluctuations in these experiments. At the center of the laser-heated spot, we will benchmark the eight-color system against the spectroradiometer. If an unforeseen issue prevents us from finishing the eight-color system in a timely manner, we will continue to use our existing system.

My experimental samples will be $Fe_{84.5}$–$Ni_{5.5}$–HSE_{10} alloys combined with synthetic mid-ocean ridge basalt (MORB) glass to approximately correspond to the Earth's core and mantle, respectively. Synthetic samples will be used to ensure sample purity. The metal alloys will be doped with up to 10% of the HSE of interest—an artificially high ratio used to ensure that the HSE content in the silicate portion of the sample is measurable after the experimental run. I will account for this later in my analysis by performing an infinite dilution correction with a Margules mixing model as in Mann et al. (2012) to calculate activity coefficients and determine accurate partition coefficients given realistic trace abundances (Mukhopadhyay et al., 1993).

First, the metal will be loaded into a piston–cylinder press in the Fischer Lab as mixtures of elemental powders, inside a stack of MgO, a graphite heater, and a $BaCO_3$ cylinder that together constitute the cell assembly. The assemblies will be inserted into the piston–cylinder stack and compressed to ~1 GPa, then electrically heated to ~1600–1800 K, significantly above the iron melting point (~1550 K). Temperatures will be measured using a Type C thermocouple, and the peak temperature will be held for several minutes to ensure melting before the samples are quenched and depressurized.

Samples will then be loaded using established DAC techniques (e.g., Blanchard et al., 2022; Fischer et al., 2015; Siebert et al., 2012; Suer et al., 2021). Each iron alloy will be extracted from the piston–cylinder cell assembly, and a small portion of it will be pressed into a foil using diamond anvils with 1000 μm culets. Rhenium gaskets will be preindented to ~30 GPa, laser-drilled to create the sample chamber, and loaded into a DAC containing diamond anvils with 300 μm culets. The metal foil will then be loaded into the sample chamber between two flakes of pressed MORB powder, which double as the thermal insulation and pressure medium. When combined, the total metal–silicate sample will initially be ~30–35 μm thick. No additional pressure medium is necessary because our target area will be molten, which greatly increases the hydrostaticity (Takemura, 2021); this helps prevent chemical contamination of the sample by an

additional component. Before closing and pressurizing, the loaded cell will be dried in a vacuum oven to remove any absorbed moisture.

Pressures will be slowly increased to a target value within the range 30–90 GPa. I will determine pressure in our samples using a confocal Raman spectroscopy system in the Fischer Lab to measure the wavenumber shift of the diamond culets. This shift in frequency of the Raman scatter compared to an initial monochromatic laser is related to the change in the diamond's molecular vibrational frequency, which can be used to quantify the pressure (Akahama & Kawamura, 2006; Boppart et al., 1985). Pressures measured before and after heating will be corrected to account for a thermal pressure contribution (e.g., Fischer et al., 2015), allowing us to estimate the pressure on the sample during the experiment.

The sample will then be laser heated by gradually increasing the temperature on both sides of the sample to above the MORB liquidus (~3600–4300 K) (Andrault et al., 2011). Once the target temperature is reached and held for several seconds to ensure equilibration (Ertel et al., 2008; Fischer et al., 2015), the sample will be rapidly quenched by shutting off the lasers. The post-run pressure will be measured before decompression, sample recovery, and chemical characterization (Section 3.2).

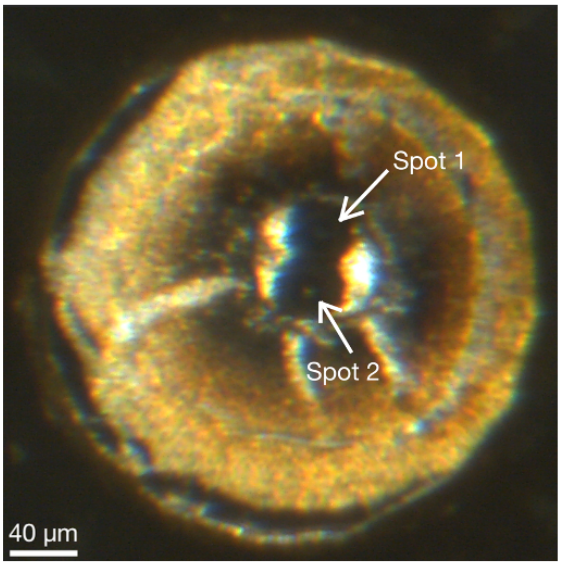

Figure 3. Image of the post-run pilot sample under reflected and transmitted light. Arrows point to the two laser-heated spots.

This process will be repeated for samples containing each of the four HSEs of interest until I have at least five successful experiments per HSE. I have performed a pilot experiment to serve as a "proof of concept" for our experimental methods and a benchmark for our analyses. This experiment contains 30% HSEs—10% each of Pt, Rh, and Ru—as opposed to the proposed 10%. This will allow us to investigate the behaviors of multiple HSEs at once. The consequent lower percentage of iron in the alloy is not an issue for this run because its sole purpose is to test whether 10% of each HSE in the starting material is enough to be able to measure its abundance in the silicate melt, though this sample may yield usable results with an adequate infinite dilution correction. Pt is included to allow comparison of our test results to the only published LH-DAC HSE partitioning data from Suer et al. (2021). Our pilot sample was synthesized in the piston–cylinder and loaded into a DAC following the steps described above. The sample was compressed to 31 GPa and two spots were laser-heated to >4300 K. It is currently awaiting post-run recovery and chemical analysis (Figure 3). If this analysis proves the concentrations are too low to reliably quantify, I will increase the HSE abundances in the proposed starting materials. Conversely, if the HSEs are easily measurable, I will decrease their starting abundances and potentially include more than one element per experiment.

3.2 Post-Run Sample Chemical Analysis

I will perform the necessary chemical analyses at the Harvard Center for Nanoscale Systems (CNS) (CNS, 2021b, 2021a, 2022). After samples are quenched and decompressed, a 3–

5 μm thick cross-section will be cut, polished, and removed from the center of a laser-heated spot on each sample using a focused ion beam field emission scanning electron microscope (FIB-SEM) with a micromanipulator. This SEM has both secondary electron and backscattered electron modes, allowing for both compositional and topographical measurements and imaging. I will use the backscattered electron images to locate the metal–silicate boundary and correlate with the eight-color temperature maps. The major and minor element and HSE abundances in the metal and silicate melts will be measured using wavelength dispersive spectroscopy (WDS) in an SEM. WDS measures the composition one element at a time, isolating only one wavelength of the X-rays released by the sample after it is blasted with an electron beam (Goodge, 2007). While slower than energy dispersive spectroscopy, WDS has significantly higher spectral resolution and reproducibility (Zinin, 2011). The partition coefficients will be calculated for each element using the mole fractions in both the metal and silicate phases, as in Equation 1.

I will also investigate quench features, including the ubiquitous metallic nuggets in the silicate. Using a 3D atom probe, the Fischer Lab is currently investigating these nanonuggets, with preliminary analyses confirming that the features' shapes and compositions are consistent with quench formation in LH-DAC metal–silicate partitioning experiments. 3D atom probe microtomography has the analytical resolution necessary to measure these compositions by using a tightly focused UV laser spot to obtain atom-by-atom identification and spatial positioning (CNS, 2022). In addition to the nanonuggets, I plan to investigate the HSE compositions near the metal–silicate boundary. By averaging concentrations over several small (~300x50 nm) regions (Figure 4), I will avoid larger-scale heterogeneities while recording accurate compositions of any unusual textural features.

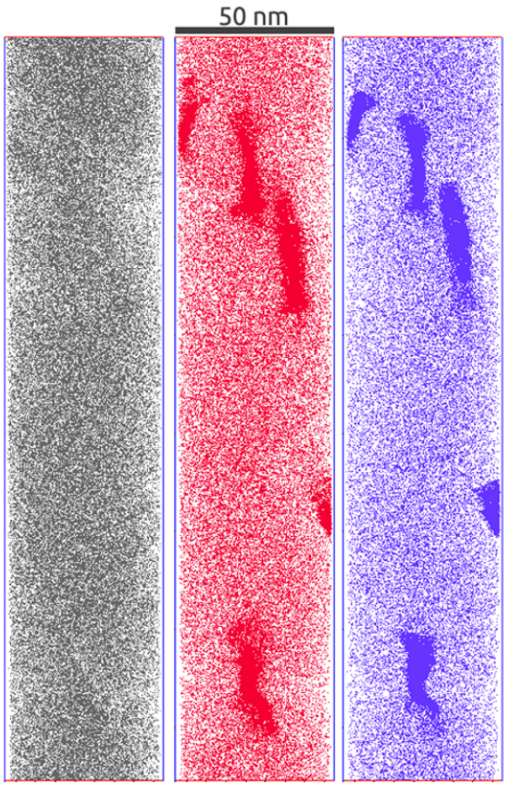

Figure 4. 3D atom probe results from ongoing Fischer Group LH-DAC experiments. Each dot represents an atom of Si (left), Fe (middle), or Pd (right).

If this combination of SEM-WDS and 3D atom probe is incapable of adequately characterizing the HSE distribution, we will analyze the sample using a nanoscale secondary ion mass spectrometer (NanoSIMS). NanoSIMS has been shown to possess the spatial and analytical resolution necessary to measure HSEs in LH-DAC samples (Suer et al., 2021). Although Harvard CNS does not have this instrument, we could potentially take advantage of a previous Fischer Group collaboration (Fischer et al., 2020). To best prepare for potential setbacks, I will begin the chemical analysis with SEM-WDS measurements, which will allow us to initially characterize the sample and determine if the run products are suitable for more destructive techniques, such as 3D atom probe or NanoSIMS analysis. These proposed analytical methods take advantage of cutting-edge technology to perform the best possible measurements and will therefore be challenging, but they are based on established methodologies successfully employed in previous LH-DAC metal–

silicate partitioning studies (e.g., Fischer et al., 2015, 2020; Siebert et al., 2013; Suer et al., 2021).

3.3 Incorporation of *N*–Body Simulations

Because the goal of these experiments is to provide more precise high *P–T* HSE partition coefficients than ever before, it is necessary to incorporate them into models that are similarly well-constrained. The resulting partitioning parameterizations will be input into an updated multi-stage core formation model (after Gu et al., 2023). To relate these geochemical constraints with realistic accretion histories of the Earth, I will utilize outputs from previously published *N*-body simulations that incorporated collisional ejecta (e.g., Crespi et al., 2021). *N*–body simulations characterize the timing, mass, and provenance of material accreted by the terrestrial planets throughout their formation by modeling the gravitational interactions between planetesimals, planetary embryos, and protoplanets (Chambers & Wetherill, 1998). A host of simulation types have been proposed to attempt to replicate the terrestrial planets' masses and orbits, with differences including the orbital evolution of Jupiter and Saturn, the radial distribution of mass, the particle size, and impact behavior (Chambers, 2004; Clement et al., 2019; Jacobson & Walsh, 2015).

While there has been extensive debate on the composition and size of late-accreted bodies, previous studies typically approximate the late veneer as being comprised of undifferentiated chondrites (Brasser et al., 2016; Fischer-Gödde et al., 2020). Incorporating growth histories from *N*-body simulations will allow us to investigate the provenances of planetesimals still remaining in the inner disk at the final stages of accretion. For example, Carter & Stewart (2022) argue that it may have been common for planetesimals that are isotopically similar to the Earth to be left in the inner disk at this point—usually as the remnants of previously ejected protoplanets. These bodies provide an alternative possible source of late-accreted HSEs that can explain both their high absolute abundances and chondritic relative proportions. Examining the full range of parameters in these planetesimals will be necessary to accurately approximate the late veneer, since previous studies have suggested that some fragment of these cores may remain in the Earth's mantle (Burger et al., 2020; Korenaga et al., 2023).

During the collisional stages of planet formation, these planetesimals may also have experienced substantial impact erosion, so using *N*-body simulations that include collisional outcomes with imperfect accretion will expand the range of potential late veneer material even further. Simulations that incorporate collisional effects do so by parameterizing smoothed-particle hydrodynamics (SPH) simulations of collisions (e.g., Crespi et al., 2021). These are applied to collisions in the *N*-body simulations based on impact angle, mass ratio, and velocity, and are used to determine material, mass, velocity, and orbits of ejecta (Cambioni et al., 2021; Crespi et al., 2021). Embryo collisions can be complex, and depending on the collisional style, the material ejected to space could be enriched in silicate from the embryo mantles/crusts as opposed to metal from their cores (Cambioni et al., 2021; Morbidelli & Wood, 2015). This is an especially important consideration for the HSEs because they are so siderophile, and it would further affect the bulk metal/silicate ratios of potential impactors available for the late veneer compared to their precursory counterparts (Haghighipour & Maindl, 2022). Due to their siderophility, the HSEs may be one of the most sensitive indicators of processes such as this, underscoring the importance of considering HSE partitioning together with simulations including collisional alterations.

To do so, I will collate a catalog of Earth analogs from *N*–body simulations that include collisional break-up models (e.g., Burger et al., 2020; Cambioni et al., 2021; Carter & Stewart, 2022; Chambers, 2013; Clement et al., 2019; Crespi et al., 2021; Haghighipour & Maindl, 2022). Earth analogs will be defined as bodies within 0.8–1.2 M_E and 0.8–1.2 AU in the final simulation outputs (Gu et al., 2023). For each analog, I will track the impact histories of accreting bodies. All planetesimals will be assigned an initial composition based on differentiation of a CI chondrite composition enriched in refractory elements at 0.1 GPa and 2000 K and an imposed $f\mathrm{O_2}$ (Fischer et al., 2017). A step function will be used to assign $f\mathrm{O_2}$ based on initial semimajor axis, with bounds set by the oxidation states of various meteorites (Rubie et al., 2015).

3.4 Core Formation Modeling

I will relate these outputs to the Earth's geochemical constraints using a sophisticated multi-stage core formation model with self-consistently evolving $f\mathrm{O_2}$ (e.g., Gu et al., 2023; Rubie et al., 2015), combined with a melt-scaling law from Nakajima et al. (2021). Generally, accretion models assume linearly increasing equilibration pressure (P_{equil}) and constant equilibrating fractions of silicate (k_{mantle}) and impactor cores (k_{core}) (Gu et al., 2023); however, these values are dependent on impact energy and geometry, which determine the volume of melting and metal–silicate equilibration conditions (Nakajima et al., 2021). For impactors larger than 0.01 M_E, impactor mass, velocity, and angle, as well as target mass, will be extracted from the *N*-body outputs and used as input parameters for the melt-scaling law, which I will use to calculate P_{equil} and k_{mantle} for each impact. The other equilibrating factor, k_{core}, is not easily constrained from the melt-scaling law and will instead be parameterized by fluid dynamics experiments (Deguen et al., 2014). Impactors smaller than 0.01 M_E are incompatible with the melt-scaling law, and they will therefore be treated with traditional P_{equil} and k_{mantle} assumptions (Nakajima et al., 2021).

To calculate Earth's core and mantle compositions following each impact, I will utilize an existing core formation code in the Fischer group from Gu et al. (2023) that includes growth histories and P_{equil} and k_{mantle} calculated from the melt-scaling law (Nakajima et al., 2021). After imposing an initial $f\mathrm{O_2}$ distribution in the disk, $f\mathrm{O_2}$ within the growing planet will self-consistently evolve as *P–T–X* changes, following the methodology of Rubie et al. (2011, 2015) and Fischer et al. (2017). Temperature of equilibration will vary based on the chondritic liquidus of Andrault et al. (2011). As our model Earth grows from the gradual accretion of bodies, we include the metal–silicate partitioning of the major, minor, and trace elements, using parameterizations of experimental data of the form:

$$\log_{10}(D_M) = a_M + \frac{b_M}{T} + c_M \frac{P}{T} + d_M \log_{10}(1 - X_{\mathrm{LE}}) + e_M \,\mathrm{NBO/T} + f_M \Delta\mathrm{IW} \qquad (2)$$

where T is the temperature (in K), P is the pressure (in GPa), X_{LE} is the mole fraction of each light element in the metal, NBO/T is the number of nonbridging oxygen atoms per tetrahedrally coordinated cation (a measure of the degree of silicate melt polymerization), ΔIW is the $f\mathrm{O_2}$ in $\log_{10}$ units relative to the iron–wüstite buffer, and a_M, b_M, c_M, d_M (for each light element), e_M, and f_M are fitted constants calculated using multiple linear regression for each element, M.

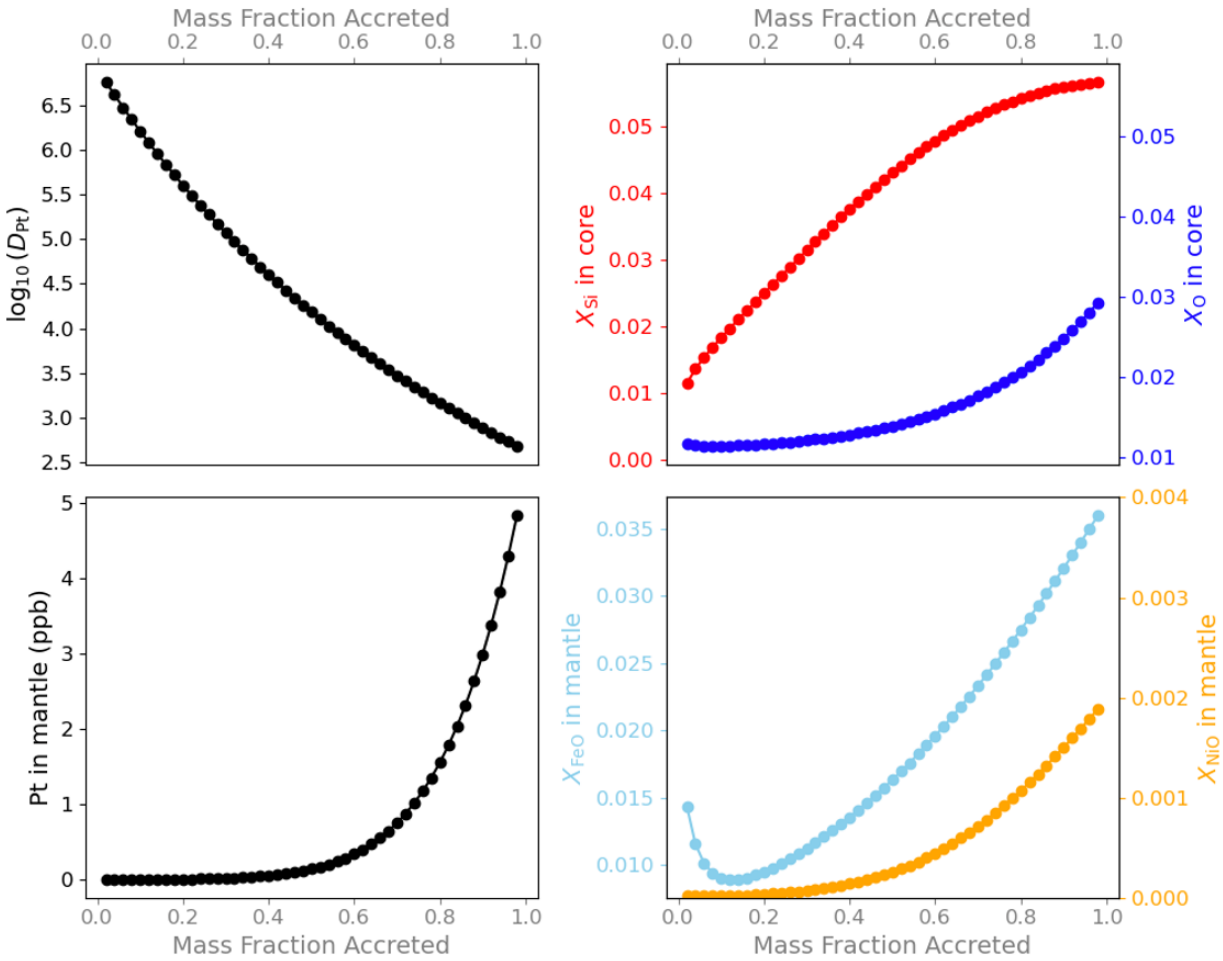

Figure 5. Multi-stage core formation model results. (0,0) Evolution of D_{Pt} during Earth formation from Equation 2 and the coefficients derived in Suer et al. (2021). (0,1) Mole fraction of Si (in red) and O (in blue) found in the core. (1,0) Evolution of mantle Pt content based on D_{Pt}. (1,1) Mole fraction of FeO (in light blue) and NiO (in orange) found in the mantle. This is a simplified model of 50 uniform impacts that does not consider *N*–body outputs and assumes linearly changing fO_2.

By using simulations that include impact ejecta and coupling them to a core formation model that includes a melt-scaling law, I intend to model a wider range of impactor sizes and provenances and potential HSE concentrations than in previous studies. I will run many iterations of the model, testing different k_{core} values and initial fO_2 distributions, as well as assigning different accretion histories to the accreting embryos based on the *N*-body outputs. Upon completion, I will compare each modeled final composition to the BSE, particularly focusing on FeO, NiO, CoO, and the Earth's core light elements to ensure our model parameters are plausible (Figure 5). Ni and Co are chosen because their partitioning behaviors are well-studied (Fischer et al., 2015) and their BSE values well-constrained (Bouhifd & Jephcoat, 2011). Their refractory siderophile nature serves as an indicator of core formation properties, tracing the Fe content in the mantle and the pressures of equilibration. If I find that an additional mechanism must be introduced in order to drawdown HSE abundances after core formation (see Scenario 3 in Section 4), I will further modify our model to include this new contribution.

4 Anticipated Results

Even with these proposed advances, this research still relies on approximations that are an intrinsic part of these experiments and models. For many of these limitations, this project will help define their importance for further study. Sulfur is known to affect the partitioning of the HSEs (Jana & Walker, 1997) and is expected to become even more siderophile with increasing *P–T*, possibly increasing its effect even further (Brenan et al., 2016; Suer et al., 2017). In order to even more accurately model conditions of Earth's core formation, HSE LH-DAC metal–silicate partitioning experiments that include sulfur will be needed. However, it is important to first characterize the partitioning of the HSEs without S. Depending on the success of our initial suite of experiments, including S in a further set of experiments would be a natural continuation of the project. The collisional effects considered in the proposed suite of *N*-body outputs, while an improvement over perfect merging, are still simplified. These simulations only consider endmember collision cases with specific masses and core mass fractions, and often neglect the effects of debris reaccretion (Cambioni et al., 2021; Crespi et al., 2021). As simulations continue to rapidly improve, these further contributions can be included in this and future works. For each impact in our model, metal–silicate equilibration is assumed to occur at a single *P* and *T*, while in reality it is expected to depend on the incorporation of the metal into the silicate and the time required for the metal to sink into the core (Deguen et al., 2014; Fischer et al., 2017). Once formed, the core is treated as completely segregated from the mantle, although it is possible that large impacts could result in some amount of remixing (Itcovitz et al., 2024). These will be important considerations as we continue to improve upon our core formation model.

Despite these assumptions and others built into our work, the combination of the higher *P–T* range of our experiments and the consideration of collisional outcomes in our modeling will significantly improve upon the results of previous studies. I anticipate our results will emphasize the joint dependence of late veneer models on Solar System dynamics and HSE partitioning behaviors. From the experimental and computational results, there may be three potential outcomes:

1. Core formation alone can explain the absolute and relative abundances of these HSEs without invoking delivery via a late veneer. Several recent studies have suggested that a late veneer is not required to explain volatile delivery to the Earth (Blanchard et al., 2022; Walker, 2009). If this holds true for the rest of the HSEs in future studies, then a late veneer may not be required to explain the BSE's composition. In this case, some late accretion may still have occurred, as suggested by dynamical studies (e.g., Raymond et al., 2013), but the geochemical signature of this material would not be as simple as an addition to the mantle with no metal–silicate equilibration as in the case of a "late veneer" (Rubie et al., 2011).

2. Core formation alone cannot explain these elements' relative and/or absolute BSE abundances, requiring the addition of chondritic material in the late veneer. Using the new HSE partition coefficients and their resulting abundances predicted by core formation models, I can calculate the difference between modeled and measured BSE compositions. The resulting mass of material delivered in the late veneer would be more accurately constrained than ever before.

3. Core formation produces HSE abundances higher than the BSE, or in moderately high but nonchondritic abundances, so an additional process is required to remove mantle HSEs. This may be the case if I find a large shift in HSE partitioning behaviors at high *P–T*, as was recently observed in Pt (Suer et al., 2021). This would necessitate a secondary process, such as Fe disproportionation (Frost et al., 2004) or sulfide segregation (Rubie et al., 2016), to deplete the

surplus mantle HSEs. In this case, a late veneer may also be required to explain the chondritic relative abundances of HSEs in the BSE, and I will be able to constrain the required late veneer mass as in Scenario 2.

These scenarios have all been suggested previously (e.g., Armstrong et al., 2019; Blanchard et al., 2022; Brasser et al., 2016; Raymond et al., 2013; Righter et al., 2008; Rudge et al., 2010; Walker, 2009). However, by combining experiments on the partitioning of multiple HSEs at the actual conditions of Earth's core formation with a sophisticated model of these processes for the first time, this proposed project will distinguish between these scenarios with a much higher degree of certainty than any prior study. While these proposed results focus on Earth's late accretion, the implications for the late veneer hypothesis will apply to terrestrial planet accretion throughout the Solar System.

5 References

Akahama, Y., & Kawamura, H. (2006). Pressure calibration of diamond anvil Raman gauge to 310 GPa. Journal of Applied Physics, 100(4). https://doi.org/10.1063/1.2335683

Andrault, D., Bolfan-Casanova, N., Nigro, G. Lo, Bouhifd, M. A., Garbarino, G., & Mezouar, M. (2011). Solidus and liquidus profiles of chondritic mantle: Implication for melting of the Earth across its history. Earth and Planetary Science Letters, 304(1–2), 251–259. https://doi.org/10.1016/j.epsl.2011.02.006

Anzellini, S., & Boccato, S. (2020). A practical review of the laser-heated diamond anvil cell for university laboratories and synchrotron applications. Crystals, 10(6). https://doi.org/10.3390/cryst10060459

Armstrong, K., Frost, D. J., McCammon, C. A., Rubie, D. C., & Boffa Ballaran, T. (2019). Deep magma ocean formation set the oxidation state of Earth's mantle. Science, 365, 903–906. https://www.science.org

Bennett, N. R. (2013). The Solubility and Metal-Silicate Partitioning of Some Highly Siderophile Elements: Implications for Core-Formation and Planetary Accretion.

Bennett, N. R., Brenan, J. M., & Koga, K. T. (2014). The solubility of platinum in silicate melt under reducing conditions: Results from experiments without metal inclusions. Geochimica et Cosmochimica Acta, 133, 422–442. https://doi.org/10.1016/j.gca.2014.02.046

Blanchard, I., Rubie, D. C., Jennings, E. S., Franchi, I. A., Zhao, X., Petitgirard, S., Miyajima, N., Jacobson, S. A., & Morbidelli, A. (2022). The metal–silicate partitioning of carbon during Earth's accretion and its distribution in the early solar system. Earth and Planetary Science Letters, 580. https://doi.org/10.1016/j.epsl.2022.117374

Boppart, H., Van Straaten, J., & Silvera, I. F. (1985). Raman spectra of diamond at high pressures. Physical Review B, 32.

Bottke, W. F., Walker, R. J., Day, J. M. D., Nesvorny, D., & Elkins-Tanton, L. (2010). Stochastic Late Accretion to Earth, the Moon, and Mars. Science, 330(6010), 1527–1530. https://doi.org/10.1126/science.1192546

Bouhifd, M. A., & Jephcoat, A. P. (2011). Convergence of Ni and Co metal-silicate partition coefficients in the deep magma-ocean and coupled silicon-oxygen solubility in iron melts at high pressures. Earth and Planetary Science Letters, 307(3–4), 341–348. https://doi.org/10.1016/j.epsl.2011.05.006

Brasser, R., Mojzsis, S. J., Werner, S. C., Matsumura, S., & Ida, S. (2016). Late veneer and late accretion to the terrestrial planets. Earth and Planetary Science Letters, 455, 85–93. https://doi.org/10.1016/j.epsl.2016.09.013

Brenan, J. M., Bennett, N. R., & Zajacz, Z. (2016). Experimental results on fractionation of the Highly Siderophile Elements (HSE) at variable pressures and temperatures during planetary and magmatic differentiation. Reviews in Mineralogy and Geochemistry, 81, 1–87. https://doi.org/10.2138/rmg.2016.81.1

Brenan, J. M., & McDonough, W. F. (2009). Core formation and metal-silicate fractionation of osmium and iridium from gold. Nature Geoscience, 2(11), 798–801. https://doi.org/10.1038/ngeo658

Brennan, M. C., Fischer, R. A., & Irving, J. C. E. (2020). Core formation and geophysical properties of Mars. Earth and Planetary Science Letters, 530. https://doi.org/10.1016/j.epsl.2019.115923

Burger, C., Bazsó, & Schäfer, C. M. (2020). Realistic collisional water transport during terrestrial planet formation: Self-consistent modeling by an N -body-SPH hybrid code. Astronomy and Astrophysics, 634. https://doi.org/10.1051/0004-6361/201936366

Cambioni, S., Jacobson, S. A., Emsenhuber, A., Asphaug, E., Rubie, D. C., Gabriel, T. S. J., Schwartz, S. R., & Furfaro, R. (2021). The effect of inefficient accretion on planetary differentiation. Planetary Science Journal, 2(3). https://doi.org/10.3847/PSJ/abf0ad

Campbell, A. J. (2008). Measurement of temperature distributions across laser heated samples by multispectral imaging radiometry. Review of Scientific Instruments, 79(1). https://doi.org/10.1063/1.2827513

Campbell, A. J., Seagle, C. T., Heinz, D. L., Shen, G., & Prakapenka, V. B. (2007). Partial melting in the iron-sulfur system at high pressure: A synchrotron X-ray diffraction study. Physics of the Earth and Planetary Interiors, 162(1–2), 119–128. https://doi.org/10.1016/j.pepi.2007.04.001

Canup, R. M. (2004). Simulations of a late lunar-forming impact. Icarus, 168(2), 433–456. https://doi.org/10.1016/j.icarus.2003.09.028

Carter, P. J., & Stewart, S. T. (2022). Did Earth Eat Its Leftovers? Impact Ejecta as a Component of the Late Veneer. Planetary Science Journal, 3(4). https://doi.org/10.3847/PSJ/ac6095

Chambers, J. E. (2001). Making More Terrestrial Planets. Icarus, 152(2), 205–224. https://doi.org/10.1006/icar.2001.6639

Chambers, J. E. (2004). Planetary accretion in the inner Solar System. Earth and Planetary Science Letters, 223(3–4), 241–252. https://doi.org/10.1016/j.epsl.2004.04.031

Chambers, J. E. (2013). Late-stage planetary accretion including hit-and-run collisions and fragmentation. Icarus, 224(1), 43–56. https://doi.org/10.1016/j.icarus.2013.02.015

Chambers, J. E., & Cassen, P. (2002). The effects of nebula surface density profile and giant-planet eccentricities on planetary accretion in the inner solar system. Meteoritics and Planetary Science, 37(11), 1523–1540. https://doi.org/10.1111/j.1945-5100.2002.tb00808.x

Chambers, J. E., & Wetherill, G. W. (1998). Making the Terrestrial Planets: N-Body Integrations of Planetary Embryos in Three Dimensions. In ICARUS (Vol. 136).

Chou, C.-L. (1978). Fractionation of siderophile elements in the earth's upper mantle. Proc. Lunar Planet Sci. Conf. , 9th, 219–230.

Clement, M. S., Kaib, N. A., Raymond, S. N., Chambers, J. E., & Walsh, K. J. (2019). The early instability scenario: Terrestrial planet formation during the giant planet instability, and the effect of collisional fragmentation. Icarus, 321, 778–790. https://doi.org/10.1016/j.icarus.2018.12.033

CNS. (2021a, September 9). FEI Helios 660. Harvard CNS. https://cns1.rc.fas.harvard.edu/tool-details?id=2442

CNS. (2021b, September 9). JEOL 7900F SEM. Harvard CNS. https://cns1.rc.fas.harvard.edu/tool-details?id=2559

CNS. (2022, September 9). 3D Atom Probe. Harvard CNS. https://cns1.rc.fas.harvard.edu/tool-details?id=2359

Cottrell, E., & Walker, D. (2006). Constraints on core formation from Pt partitioning in mafic silicate liquids at high temperatures. Geochimica et Cosmochimica Acta, 70(6), 1565–1580. https://doi.org/10.1016/j.gca.2005.11.021

Crespi, S., Dobbs-Dixon, I., Georgakarakos, N., Haghighipour, N., Maindl, T. I., Schäfer, C. M., & Winter, P. M. (2021). Protoplanet collisions: Statistical properties of ejecta. Monthly Notices of the Royal Astronomical Society, 508(4), 6013–6022. https://doi.org/10.1093/mnras/stab2951

Danielson, L. R., Sharp, T. G., & Hervig, R. L. (2005). IMPLICATIONS FOR CORE FORMATION OF THE EARTH FROM HIGH PRESSURE-TEMPERATURE AU PARTITIONING EXPERIMENTS. Lunar and Planetary Science, 1–2.

Day, J. M. D., Brandon, A. D., & Walker, R. J. (2016). Highly siderophile elements in Earth, Mars, the Moon, and Asteroids. In Highly Siderophile and Strongly Chalcophile Elements in High-Temperature Geochemistry and Cosmochemistry (pp. 161–238). De Gruyter. https://doi.org/10.2138/rmg.2016.81.04

Deguen, R., Landeau, M., & Olson, P. (2014). Turbulent metal-silicate mixing, fragmentation, and equilibration in magma oceans. Earth and Planetary Science Letters, 391, 274–287. https://doi.org/10.1016/j.epsl.2014.02.007

Deguen, R., Olson, P., & Cardin, P. (2011). Experiments on turbulent metal-silicate mixing in a magma ocean. Earth and Planetary Science Letters, 310(3–4), 303–313. https://doi.org/10.1016/j.epsl.2011.08.041

Ertel, W., O'Neill, H. St. C., Sylvester, P. J., & Dingwell, D. B. (1999). Solubilities of Pt and Rh in a haplobasaltic silicate melt at 1300ºC. Geochimica et Cosmochimica Acta, 63, 2439-2499.

Ertel, W., Dingwell, D. B., & Sylvester, P. J. (2008). Siderophile elements in silicate melts - A review of the mechanically assisted equilibration technique and the nanonugget issue. Chemical Geology, 248(3–4), 119–139. https://doi.org/10.1016/j.chemgeo.2007.12.013

Fischer, R. A., & Campbell, A. J. (2010). High-pressure melting of wüstite. American Mineralogist, 95(10), 1473–1477. https://doi.org/10.2138/am.2010.3463

Fischer, R. A., Campbell, A. J., & Ciesla, F. J. (2017). Sensitivities of Earth's core and mantle compositions to accretion and differentiation processes. Earth and Planetary Science Letters, 458, 252–262. https://doi.org/10.1016/j.epsl.2016.10.025

Fischer, R. A., Cottrell, E., Hauri, E., M Lee, K. K., & Le Voyer, M. (2020). The carbon content of Earth and its core. PNAS, 117(16), 8743–8749. https://doi.org/10.1073/pnas.1919930117/-/DCSupplemental

Fischer, R. A., Nakajima, Y., Campbell, A. J., Frost, D. J., Harries, D., Langenhorst, F., Miyajima, N., Pollok, K., & Rubie, D. C. (2015). High pressure metal-silicate partitioning of Ni, Co, V, Cr, Si, and O. Geochimica et Cosmochimica Acta, 167, 177–194. https://doi.org/10.1016/j.gca.2015.06.026

Fischer-Gödde, M., Elfers, B. M., Münker, C., Szilas, K., Maier, W. D., Messling, N., Morishita, T., Van Kranendonk, M., & Smithies, H. (2020). Ruthenium isotope vestige of Earth's pre-late-veneer mantle preserved in Archaean rocks. Nature, 579(7798), 240–244. https://doi.org/10.1038/s41586-020-2069-3

Fischer-Gödde, M., & Kleine, T. (2017). Ruthenium isotopic evidence for an inner Solar System origin of the late veneer. Nature, 541(7638), 525–527. https://doi.org/10.1038/nature21045

Frost, D. J., Liebske, C., Langenhorst, F., McCammon, C. A., Tronnes, R. G., & Rubie, D. C. (2004). Experimental evidence for the existence of iron-rich metal in the Earth's lower mantle. Nature, 428(6981), 406–409. https://doi.org/10.1038/nature02309

Goodge, J. (2007, May 17). Energy-Dispersive X-Ray Spectroscopy (EDS) How it Works-EDS. https://serc.carleton.edu/research_education/geochemsheets/eds.html

Gu, J. T., Fischer, R. A., Brennan, M. C., Clement, M. S., Jacobson, S. A., Kaib, N. A., O'Brien, D. P., & Raymond, S. N. (2023). Comparisons of the core and mantle compositions of earth analogs from different terrestrial planet formation scenarios. Icarus, 394. https://doi.org/10.1016/j.icarus.2023.115425

Haghighipour, N., & Maindl, T. I. (2022). Building Terrestrial Planets: Why Results of Perfect-merging Simulations Are Not Quantitatively Reliable Approximations to Accurate Modeling of Terrestrial Planet Formation. The Astrophysical Journal, 926(2), 197. https://doi.org/10.3847/1538-4357/ac4969

Itcovitz, J. P., Rae, A. S. P., Davison, T. M., Collins, G. S., & Shorttle, O. (2024). The Distribution of Impactor Core Material During Large Impacts on Earth-like Planets. Planetary Science Journal, 5(4). https://doi.org/10.3847/PSJ/ad2ea4

Jacobson, S. A., & Walsh, K. J. (2015). Earth and Terrestrial Planet Formation. In The Early Earth: Accretion and Differentiation (pp. 49–70). https://doi.org/10.1002/9781118860359.ch3

Jana, D., & Walker, D. (1997). The influence of sulfur on partitioning of siderophile elements. In Geochimica et Cosmoehimica Acta (Vol. 61, Issue 24).

Kendall, J. D., & Melosh, H. J. (2016). Differentiated planetesimal impacts into a terrestrial magma ocean: Fate of the iron core. Earth and Planetary Science Letters, 448, 24–33. https://doi.org/10.1016/j.epsl.2016.05.012

Kimura, K., Lewis, R. S., & Anders, E. (1974). Distribution of gold and rhenium between nicke–iron and silicate melts: implications for the abundance of siderophile elements on the Earth and Moon. Geochimica et Cosmochimica Acta, 38, 683–701.

Korenaga, J., Marchi, S., & Edited by Richard Walker, I. (2023). Vestiges of impact-driven three-phase mixing in the chemistry and structure of Earth's mantle. PNAS 120. https://doi.org/10.1073/pnas.2309181120

Lichtenberg, T., Schaefer, L. K., Nakajima, M., & Fischer, R. A. (2022). Geophysical Evolution During Rocky Planet Formation. ArXiv. http://arxiv.org/abs/2203.10023

Mann, U., Frost, D. J., Rubie, D. C., Becker, H., & Audétat, A. (2012). Partitioning of Ru, Rh, Pd, Re, Ir and Pt between liquid metal and silicate at high pressures and high temperatures - Implications for the origin of highly siderophile element concentrations in the Earth's mantle. Geochimica et Cosmochimica Acta, 84, 593–613. https://doi.org/10.1016/j.gca.2012.01.026

Marchi, S., Canup, R. M., & Walker, R. J. (2018). Heterogeneous delivery of silicate and metal to the Earth by large planetesimals. Nature Geoscience, 11(1), 77–81. https://doi.org/10.1038/s41561-017-0022-3

McDonough, W. F., & Sun, S. (1995). The composition of the Earth. Chemical Geology, 120, 223–253.

Médard, E., Schmidt, M. W., Wälle, M., Keller, N. S., & Günther, D. (2015). Platinum partitioning between metal and silicate melts: Core formation, late veneer and the nanonuggets issue. Geochimica et Cosmochimica Acta, 162, 183–201. https://doi.org/10.1016/j.gca.2015.04.019

Morbidelli, A., Lunine, J. I., O'Brien, D. P., Raymond, S. N., & Walsh, K. J. (2012). Building terrestrial planets. In Annual Review of Earth and Planetary Sciences (Vol. 40, pp. 251–275). https://doi.org/10.1146/annurev-earth-042711-105319

Morbidelli, A., & Wood, B. (2015). Late Accretion and the Late Veneer. In The Early Earth: Accretion and Differentiation (pp. 71–82). https://doi.org/10.1002/9781118860359.ch4

Mukhopadhyay, B., Sabyasachi Basu, I., & Holdaway, M. J. (1993). A discussion of Margules-type formulations for multicomponent solutions with a generalized approach. Geochimica et Cosmochimica Acta, 57, 277–283.

Nakajima, M., Golabek, G. J., Wünnemann, K., Rubie, D. C., Burger, C., Melosh, H. J., Jacobson, S. A., Manske, L., & Hull, S. D. (2021). Scaling laws for the geometry of an impact-induced magma ocean. Earth and Planetary Science Letters, 568. https://doi.org/10.1016/j.epsl.2021.116983

Nimmo, F., & Kleine, T. (2015). Early Differentiation and Core Formation: Processes and Timescales. In The Early Earth: Accretion and Differentiation (pp. 83–102).

O'Brien, D. P., Morbidelli, A., & Levison, H. F. (2006). Terrestrial planet formation with strong dynamical friction. Icarus, 184(1), 39–58. https://doi.org/10.1016/j.icarus.2006.04.005

Palme, H., & O'Neill, H. (2013). Cosmochemical Estimates of Mantle Composition. In Treatise on Geochemistry: Second Edition (Vol. 3, pp. 1–39). Elsevier Inc. https://doi.org/10.1016/B978-0-08-095975-7.00201-1

Raymond, S. N., Schlichting, H. E., Hersant, F., & Selsis, F. (2013). Dynamical and collisional constraints on a stochastic late veneer on the terrestrial planets. Icarus, 226(1), 671–681. https://doi.org/10.1016/j.icarus.2013.06.019

Righter, K., Humayun, M., & Danielson, L. (2008). Partitioning of palladium at high pressures and temperatures during core formation. Nature Geoscience, 1(5), 321–323. https://doi.org/10.1038/ngeo180

Righter, K., & O'Brien, D. P. (2011). Terrestrial planet formation. PNAS. https://doi.org/10.1073/pnas.1013480108/-/DCSupplemental

Ringwood, A. E. (1966). Chemical evolution of the terrestrial planets. Geochimica et Cosmochimica Acta, 30, 41–104.

Rubie, D. C., Frost, D. J., Mann, U., Asahara, Y., Nimmo, F., Tsuno, K., Kegler, P., Holzheid, A., & Palme, H. (2011). Heterogeneous accretion, composition and core-mantle differentiation of the Earth. Earth and Planetary Science Letters, 301(1–2), 31–42. https://doi.org/10.1016/j.epsl.2010.11.030

Rubie, D. C., Jacobson, S. A., Morbidelli, A., O'Brien, D. P., Young, E. D., de Vries, J., Nimmo, F., Palme, H., & Frost, D. J. (2015). Accretion and differentiation of the terrestrial planets with implications for the compositions of early-formed Solar System bodies and accretion of water. Icarus, 248, 89–108. https://doi.org/10.1016/j.icarus.2014.10.015

Rubie, D. C., Laurenz, V., Jacobson, S. A., Morbidelli, A., Palme, H., Vogel, A. K., & Frost, D. J. (2016). Highly siderophile elements were stripped from Earth's mantle by iron sulfide segregation. Science, 353(6304), 1141–1144.

Rubie, D. C., Melosh, H. J., Reid, J. E., Liebske, C., & Righter, K. (2003). Mechanisms of metal–silicate equilibration in the terrestrial magma ocean. Earth and Planetary Science Letters, 205, 239–255. www.elsevier.com/locate/epsl

Rudge, J. F., Kleine, T., & Bourdon, B. (2010). Broad bounds on Earths accretion and core formation constrained by geochemical models. Nature Geoscience, 3(6), 439–443. https://doi.org/10.1038/ngeo872

Schlichting, H. E., Warren, P. H., & Yin, Q. Z. (2012). The last stages of terrestrial planet formation: Dynamical friction and the late veneer. Astrophysical Journal, 752(1). https://doi.org/10.1088/0004-637X/752/1/8

Siebert, J., Badro, H., Antonangeli, D., & Ryerson, F. J. (2013). Terrestrial Accretion Under Oxidizing Conditions. Science, 339(6124), 1194–1197. https://doi.org/10.1126/science.1228602

Siebert, J., Badro, J., Antonangeli, D., & Ryerson, F. J. (2012). Metal-silicate partitioning of Ni and Co in a deep magma ocean. Earth and Planetary Science Letters, 321–322, 189–197. https://doi.org/10.1016/j.epsl.2012.01.013

Siebert, J., Corgne, A., & Ryerson, F. J. (2011). Systematics of metal-silicate partitioning for many siderophile elements applied to Earth's core formation. Geochimica et Cosmochimica Acta, 75(6), 1451–1489. https://doi.org/10.1016/j.gca.2010.12.013

Siebert, J., & Shahar, A. (2015). An Experimental Geochemistry Perspective on Earth's Core Formation. In The Early Earth: Accretion and Differentiation (pp. 103–121). wiley. https://doi.org/10.1002/9781118860359.ch6

Suer, T. A., Siebert, J., Remusat, L., Day, J. M. D., Borensztajn, S., Doisneau, B., & Fiquet, G. (2021). Reconciling metal–silicate partitioning and late accretion in the Earth. Nature Communications, 12(1). https://doi.org/10.1038/s41467-021-23137-5

Suer, T. A., Siebert, J., Remusat, L., Menguy, N., & Fiquet, G. (2017). A sulfur-poor terrestrial core inferred from metal–silicate partitioning experiments. Earth and Planetary Science Letters, 469, 84–97. https://doi.org/10.1016/j.epsl.2017.04.016

Takemura, K. (2021). Hydrostaticity in high pressure experiments: some general observations and guidelines for high pressure experimenters. High Pressure Research, 41(2), 155–174. https://doi.org/10.1080/08957959.2021.1903457

Wade, J., & Wood, B. J. (2005). Core formation and the oxidation state of the Earth. Earth and Planetary Science Letters, 236(1–2), 78–95. https://doi.org/10.1016/j.epsl.2005.05.017

Walker, R. J. (2009). Highly siderophile elements in the Earth, Moon and Mars: Update and implications for planetary accretion and differentiation. Chemie Der Erde, 69(2), 101–125. https://doi.org/10.1016/j.chemer.2008.10.001

Walter, M. J., Newsom, H. E., Ertel, W., & Holzheid, A. (2000). Siderophile Elements in the Earth and Moon: Metal/Silicate Partitioning and Implications for Core Formation. In Origin of the Earth and Moon (pp. 265–290). University of Arizona Press. https://muse.jhu.edu/book/85538

Wood, B. J., Smythe, D. J., & Harrison, T. (2019). The condensation temperatures of the elements: A reappraisal. American Mineralogist, 104(6), 844–856. https://doi.org/10.2138/am-2019-6852CCBY

Zinin, P. (2011). GG 711: Microanalysis in Electron Microscopy. http://soest.hawaii.edu/HIGP/Faculty/sksharma//GG711/GG711Lec14EDS.pdf